Chemical Engineering Journal 534 (2026) 175127

Contents lists available at ScienceDirect

Chemical Engineering Journal

journal homepage: www.elsevier.com/locate/cej

Chemical and beam instability of $Na_{3.4}Zr_2Si_{2.4}P_{0.6}O_{12}$ NaSICON electrolyte for all-solid-state sodium batteries

Alexander Thomas [a,*], Björn Pohle [a], Martin Hantusch [a], Johannes Schultz [a], Stas Avdoshenko [a], Ronny Buckan [a], Lars Giebeler [a], Thomas Mühl [a], Monika Bhardwaj [b,f], Frank Tietz [b,c], Jörg Feller [d], Stefan Kaskel [e], Daria Mikhailova [a,g,*]

[a] *Leibniz Institute for Solid State and Materials Research (IFW) Dresden e. V., Helmholtzstraße 20, D-01069, Dresden, Germany*
[b] *Forschungszentrum Jülich GmbH, Institute of Energy Materials and Devices, IMD-2: Materials Synthesis and Processing, D-52425, Jülich, Germany*
[c] *Forschungszentrum Jülich GmbH, Institute of Energy Materials and Devices, IMD-4: Helmholtz Institute Münster – Ionics in Energy Storage, 52425, Jülich, Germany*
[d] *Faculty of Agriculture, Environment & Chemistry, University of Applied Sciences Dresden, D-01069, Dresden, Germany*
[e] *Department of Inorganic Chemistry, Technische Universität Dresden, Bergstraße 66, D-01069, Dresden, Germany*
[f] *Albert-Ludwigs-Universität Freiburg, Institut für Anorganische und Analytische Chemie, Albertstraße 21, 79104, Freiburg, Germany*
[g] *Karlsruhe Institute of Technology (KIT), Institute for Applied Materials (IAM), Hermann-von-Helmholtz-Platz 1, D-76344, Eggenstein-Leopoldshafen, Germany*

ARTICLE INFO

Keywords:
Sodium metal batteries
Solid-state electrolyte
NaSICON
Electron beam damage
X-ray beam damage

ABSTRACT

Development of solid-state electrolytes (SSE) is the basis to establish safe and reliable sodium batteries on the market. Despite their advantages, including non-flammable components and reduced reactivity with metallic sodium, many crystalline SSEs suffer from increased charge transfer resistance, sodium dendrite formation, and lower sodium ion conductivity compared to liquid electrolytes. To optimize SSE properties, comprehensive studies of the SSE surface in its pristine state and after contact with metallic sodium during battery operation are desirable.

In this work, the surface of pellets with the NaSICON-type $Na_{3.4}Zr_2Si_{2.4}P_{0.6}O_{12}$ composition, which is considered as a promising SSE for sodium batteries, was investigated in detail using conventional surface analytical techniques. Grazing-incidence X-ray diffraction revealed that the subsurface region of the as-prepared pellets consists of several crystalline NaSICON phases and amorphous ternary oxides, extending to a depth of approximately 1 µm. In contrast, after grinding the pellet, only one NaSICON phase could be detected using the transmission XRD technique. The chemical composition of the surface appeared to change after contact with metallic sodium, particularly for the Si-, P- and O-species. Furthermore, we observed surface instability under electron beam exposure during electron microscopy and spectroscopy measurements over 30–60 min, leading to the formation of metallic sodium on the irradiated surface area. The irradiation with X-rays during photoelectron spectroscopy measurements for several hours induced sodium depletion within the irradiated spot while depositing metallic sodium radially around the irradiated area. These findings demonstrate the restricted application of surface analytical techniques for studying ternary oxides in the Na-Zr-Si-P-O system, especially when using NaSICON as a solid electrolyte.

1. Introduction

Lithium-ion batteries (LIBs) have become the standard for mobile energy storage systems, with a significant amount of research focused on enhancing their properties such as energy density and overall performance [1]. However, the increasing demand for lithium and limitations in annual lithium production [2], [3] necessitate the exploration of alternative systems. Consequently, sodium batteries have gained interest among researchers and developers worldwide [4].

As a result, considerable progress has been made in developing and improving cathodes, anodes, and electrolytes to achieve industrially processed sodium batteries [5], [6]. Despite this progress, the major safety concern related to liquid electrolytes, remains a challenge for both lithium and sodium batteries [7], [8]. In response to strategies aimed at enhancing safety [9], the development of solid-state batteries has been pursued, with a clear roadmap for their advancement [10]. A key

---

* Corresponding authors.
E-mail addresses: alexander.thomas@ifw-dresden.de (A. Thomas), d.mikhailova@ifw-dresden.de (D. Mikhailova).

https://doi.org/10.1016/j.cej.2026.175127
Received 22 November 2025; Received in revised form 27 January 2026; Accepted 10 March 2026

component in sodium solid-state batteries (SSSBs) is the solid electrolyte, which can be composed of various compounds, such as β-aluminas [11], [12], ternary oxides like $Na_5YSi_4O_{12}$ [13], sulfides [14], boranes [15], solid-state polymers [16], or NaSICON-type materials [17], [18].

The high ionic conductivity of NaSICONs, with values reaching up to 10^{-3} S cm^{-1} at room temperature, highlights them among other potential solid electrolytes. Here, the $Na_{3.4}Zr_2Si_{2.4}P_{0.6}O_{12}$ composition exhibits the highest conductivity [19], [20]. Therefore, extensive research has been conducted on the thermal and compositional stability of phases within the ternary Na-Zr-Si-P-O system, particularly for the $Na_{1+x}Zr_2Si_xP_{3-x}O_{12}$ ($0 \leq x \leq 3$) compositions. The stability in contact with metallic sodium was especially important, because NaSICON was considered as a possible solid electrolyte for Na—S batteries at 300 °C [21]. At this temperature, both monoclinic and rhombohedral modifications of $Na_3Zr_2Si_2PO_{12}$ have been observed to coexist. The rhombohedral modification of NaSICON was likely unstable against sodium metal under these conditions and transformed into the monoclinic form, resulting in appearance of cracks and pores in the material due to volume changes upon phase transition [22]. Theoretical studies have shown that various NaSICON compositions have a low chemical stability with respect to Na metal, which is rather temperature-independent: even at room temperature, all compositions of the solid solution $Na_{1+x}Zr_2Si_xP_{3-x}O_{12}$ ($0 \leq x \leq 3$) would react with metallic sodium.

Further, thermal behavior of $Na_{1+x}Zr_2Si_xP_{3-x}O_{12}$ NaSICON materials towards phase segregation was evaluated, mostly with theoretical calculations [23]. A miscibility gap for the solid solution below 615 K was predicted, although this prognosis has been experimentally proven only once [24], due to the slow kinetics of transformations. At room temperature, the entire series of $Na_{1+x}Zr_2Si_xP_{3-x}O_{12}$ ($0 \leq x \leq 3$) might be stable without phase segregation due to kinetic reasons [25]. A recent work from 2020 revealed a complexity of phase relationships for $Na_{1+x}Zr_2Si_xP_{3-x}O_{12}$ with $0 \leq x \leq 3$, including a calculated phase diagram that shows three stable NASICON compositions at room temperature with $x = 0$, $x = 2$, and $x = 3$ [26]. Notably, the composition with $x = 2$ demonstrates a broad nonstoichiometric range, being stable within $1.5 \leq x \leq 2.0$. A structural phase transition from monoclinic to rhombohedral form at 157.7 °C for this composition was also discussed [27].

Until 2020, the $Na_{1+x}Zr_2Si_xP_{3-x}O_{12}$ system was investigated only sporadically as a potential candidate for room-temperature battery applications [19], [28]. The primary focus was on possible Na-dendrite formation at the interface with NASICON, described as black dots at the surface and a black-tinted, network-like structure in the bulk of the NaSICON pellet. These features emerged during cycling with sodium as a counter electrode [18], but a detailed examination of the black colorations is still missing, especially in light of their unusual properties compared to metallic sodium.

The information about the solid electrolyte/electrode interface, which is a key factor for the fast ion transport and entire battery performance, can be gained using surface-oriented microscopy and spectroscopy characterization techniques, which, however, could be sample-destructive.

Therefore, the stability of NaSICON under electron and X-ray beams is the other important consideration that needs to be evaluated. While the damage of NaSICON during scanning electron microscopy (SEM) investigations has previously been reported [22], it is also possible that other methods such as Auger electron spectroscopy (AES) may destruct the surface and subsurface region of the material, affecting the results of the analysis. Specifically, beam-induced sodium ion enrichment on ceramic surfaces has been reported in AES studies [29], [30] and formation of sodium metal during electron probe microanalysis [31]. In X-ray photoelectron spectroscopy (XPS) analysis, charging effects represent a significant concern despite various methods to mitigate these issues that can impact spectrum interpretation, especially for insulating materials [32], [33]. Furthermore, beam damage during XPS analysis has also been documented in ceramics [34].

In the present manuscript, we report on investigations of the surface properties of the NASICON-type $Na_{3.4}Zr_2Si_{2.4}P_{0.6}O_{12}$ composition and its interface with metallic sodium. The impact of instrumentally induced material damage was also examined to achieve reliable results. The effects of phase segregation, beam and electric field sensitivity, and electrochemical instability against metallic sodium were explored. To characterize the NaSICON material, various surface-sensitive techniques like energy-dispersive X-ray spectroscopy (EDX), AES, XPS, and bulk-sensitive techniques including X-ray diffraction (XRD), transmission electron microscopy (TEM) and electron energy loss spectroscopy (EELS) were employed. Our findings indicate that the NaSICON surface is not entirely stable when subjected to spectroscopic methods, which limits the interpretation of XPS, AES, or EDX spectra.

2. Materials and methods

2.1. Preparation of NaSICON

The synthesis of NaSICON powder has been reported elsewhere [35], [36]. For tape casting, an alcohol-based suspension was prepared using the $Na_{3.4}Zr_2Si_{2.4}P_{0.6}O_{12}$ (NaSICON) ceramic powder. The suspension comprised an azeotropic mixture of ethanol (67 vol%) and methyl ethyl ketone (33 vol%), and organic additives such as 5 wt% polyvinyl butyral (PVB-98) as a binder, and 3 wt% of Solusolve® 2075 (Solutia Inc.) and 2 wt% of PEG400® (Merck) as plasticizers. A sterically stabilizing copolymer containing multiple adsorbing anchoring groups was chosen as a dispersing agent, which is compatible with the binder and plasticizer. To achieve homogenized dispersion, the slurry was mixed in a planetary mixer at 1500 rpm for 8 min and continuously ball milled for 12 h. Finally, to eliminate bubbles, the slurry was degassed by stirring in a vacuum chamber for 2 h.

2.2. Tape casting and sintering process

The slurry was tape-cast on a polymeric foil with a slit height of 700 μm with a doctor blade, resulting in a densified layer of approximately 250 μm. The sintering process, a critical factor in ceramic processing, influences the variation in grain size, shape, and morphology. Samples with diameters of either 10 or 13 mm were punched out from the dried green tape and slowly heated to 600 °C for 2 h to remove all organic components. Subsequently, final sintering was performed at 1250 °C for 4 h. During this process, the samples were sandwiched between two NaSICON pellets to ensure flatness, a crucial aspect for cell assembly and electrochemical testing.

2.3. Structural characterizations

XRD measurements, including operando measurements, were conducted using monochromatic Mo-Kα_1 radiation ($\lambda = 0.7093$ Å) at a STOE STADI/P powder diffractometer, operated in transmission mode and a range between $2° \leq 2\theta \leq 50°$.

Grazing incidence diffraction was performed with a Philips XPert diffractometer (The Netherlands), equipped with a x-y-z stage on an Eulerian cradle, a primary beam monochromator, and a Pixcel 3D detector. Cu-Kα_1 radiation ($\lambda = 1.5406$ Å) was applied for measurements taken within the range of $4° \leq 2\theta \leq 80°$ at incidence angles of 0°, 0.005°, 0.01°, 0.05°, 0.1°, 0.5°, 1°, 2°, and 4°.

Le Bail analysis of diffraction patterns recorded at different grazing incidence angles, was performed using the Fullprof Software. [37] The refined parameters in the structural model for each measurement included unit cell metrics, zero shift (in case of two phases, zero shift was considered individually for each phase), peak shape profile (with Npr = 7, corresponding to the Thompson-Cox-Hastings pseudo-Voigt function convoluted with axial divergence asymmetry function), and the background.

For the XPS studies, a SPECS Phoibos 150 instrument with monochromatic Al-Kα (120 W) radiation was used. The measurement spot size was 3.5 mm. The AES and EDX measurements were performed on a JEOL JAMP 9500 instrument. All SEM pictures were taken with the AES device, too.

A Thermo Fisher Scientific Helios 5 CX device was used for the Focused-Ion-Beam (FIB)-cut.

TEM and STEM-EELS measurements are carried out with a double corrected FEI Titan^3 electron microscope operated at 300 kV which is equipped with a GATAN Tridiem energy filter. The STEM-EELS data were recorded using a probe semi-convergence angle of 21.5 mrad, a filter entrance aperture of 2.5 mm, a camera length of 360 mm as well as a dispersion of 1 eV.

The analysis of EELS data was carried out with the Gatan EELS analysis software package. Within this package the background was modeled and subtracted by fitting the following power laws i) a combined background around the three overlapping edges of Si, P, and Zr and ii) individual power laws around the O and the Na edge.

2.4. Atomic force microscopy (AFM)

Surface conductivity measurements were performed using conductive atomic force microscopy (C-AFM), also known as spreading resistance imaging. The measurements were conducted with a Bruker Dimension Icon scanning probe microscope equipped with conductive diamond-coated Si-cantilevers (Bruker, DDESP-FM-V2; n-doped silicon; spring constant k = 6 N/m). Topography, cantilever deflection, and tip-sample current were recorded simultaneously during contact mode scans.

2.5. Density functional theory (DFT) calculations

Optimal geometries of all molecular systems were assessed at the DFT/PBE level of theory using the Vienna Ab initio Simulation Package (VASP) [38] and projector augmented-wave method as implemented in the v5.5.4 code and the standard pseudopotential [39], [40]. The geometries were optimized in the G-point. Local Bader charges were computed using the Bader code [41]. Charged density manipulations were done using in-house Python scripts and ASE-python libraries [42].

3. Results

3.1. Analysis of the NaSICON surface with XRD and STEM-EELS

Surface morphology and phase composition of the NaSICON pellet were analyzed using STEM-EELS and grazing incidence diffraction (Fig. 1a-d). A FIB lamella was cut out near the surface of the pellet, which was then examined using HR-TEM and STEM-EELS.

Visual appearance indicated that NaSICON crystals, representing dark dots, were embedded within another phase (white structure) as seen in (Fig. 1a). The STEM-EELS analysis of P, Si and Zr (see Fig. S1) revealed significant inhomogeneity of elemental distribution in the subsurface region, with at least three different zones present at the surface. The first phase contained only Si (Fig. 1a, blue), while the darker region at the bottom incorporated P, Zr and some Si with a higher P (Fig. 1a, pink) than Zr (Fig. 1a, light blue) amount. A third region left and right to the grey band-like structure containing P and Zr with a higher Zr amount.

An in-depth investigation of the NaSICON phase revealed an egg-like shape of the crystallites (see Fig. S2 for details). The length of the crystals ranged from 20 nm to 30 nm, with width between 10 nm and 15 nm. Further surface investigation of the NaSICON pellet was conducted using grazing incidence diffraction measurements (Fig. 1b-d), which doubtlessly confirmed non-homogeneity in phase distribution in the subsurface region.

Evaluation of a possible correlation between the composition x and cell metrics of the Na$_{1+x}$Zr$_2$Si$_x$P$_{3-x}$O$_{12}$ structure at room temperature from the literature showed nearly a linear increase of the lattice parameter "*a*" with the Si-amount, but large variations and a maximum around $x \approx 2$ for the lattice parameter "*c*" in the rhombohedral setting ($R\bar{3}c$ space group, $a_m = \sqrt{3}\,a_r$) [26], [43], [44]. Probably, a non-homogeneous sodium distribution in structural voids has a strong impact on the crystal structure along the "*c*" direction, leading to a big value spreading.

As known, analysis of grazing incidence diffraction data has some limitations in comparison to the θ-2θ geometry [45], originating from an instrumentally caused peak broadening and peak shift depending on the

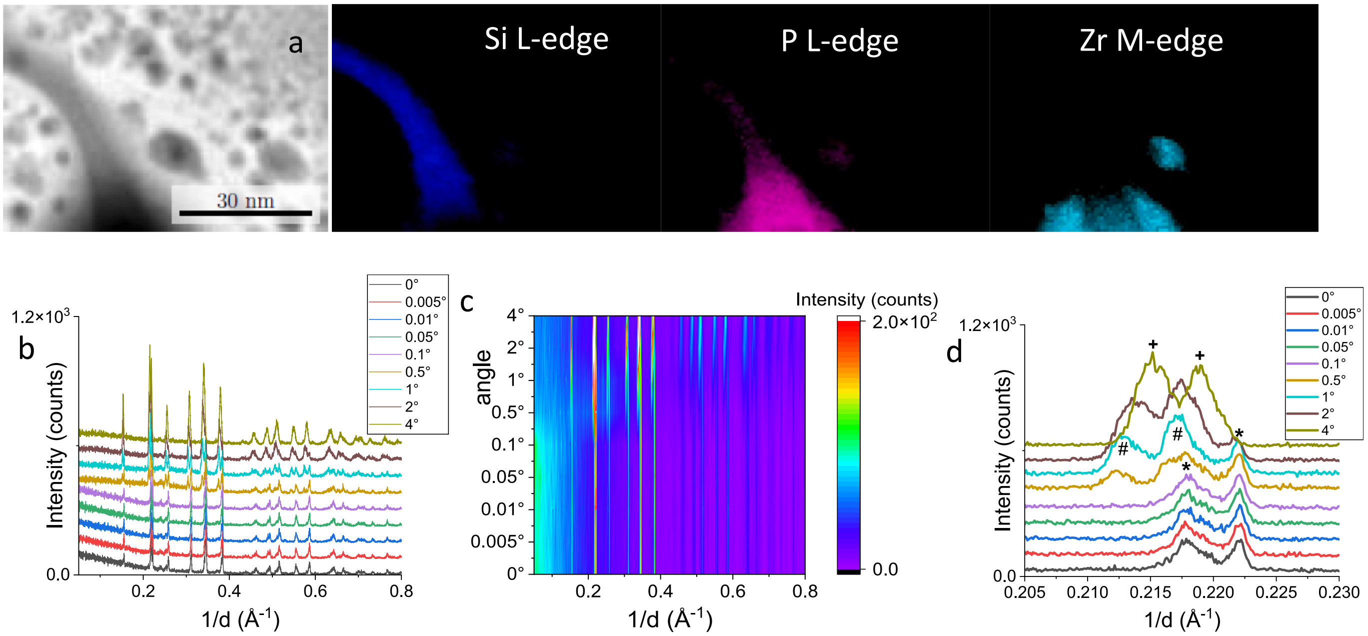

Fig. 1. *a) STEM-EELS out of a FIB lamella near the surface. Three different phases could be identified. Besides the NaSICON composition, a phase without Zr and P, and a phase without Zr are present near the surface. b) Grazing incidence diffraction of a NaSICON pellet at various grazing incidence angles, c) grazing incidence diffraction results as a counterplot, and (d) designation of three possible NaSICON phases. 1° corresponds to nearly 250 nm in depth of the pellet. Marked phases correspond to the compositions * "*Na$_2$Zr$_2$SiP$_2$O$_{12}$*", # "*Na$_{3.9}$Zr$_2$Si$_{2.9}$P$_{0.1}$O$_{12}$*", + "*Na$_{3.6}$Zr$_2$Si$_{2.6}$P$_{0.4}$O$_{12}$*". For structural information of these phases see section 2 in the Supporting Information.*

angle of incidence. Therefore, we further analyzed only relative changes in lattice parameters of NaSICON at various pellet depths, using the Le Bail method [46]. For estimation of the phase composition at each grazing incidence angle, we used the correlation between parameters "*a*", "*c*", and x in $Na_{1+x}Zr_2Si_xP_{3-x}O_{12}$, created on the basis of several structural works available in the literature [26], [43], [44].

For data analysis, we assume that the phase compositions can change only within the Na/Si/P fractions, with preserving the main structure type and the Zr/O ratio in the structure of 2/12. This conclusion is based on similarities in the diffraction patterns from the regions of the pellet close to the surface and in a depth > 1 μm. Due to the peak broadening, we cannot distinguish reliably between the monoclinic ($C2/c$) and rhombohedral modifications, which have a group-subgroup relationship. Therefore, we analyzed all data in the monoclinic $C2/c$ space group.

A monoclinic phase with almost constant composition is present at the surface and in the subsurface layer of about 25 nm thickness (the grazing incidence angle between 0° to 0.1°), see Fig. 1d. The Le Bail analysis of lattice parameters using information from [47] revealed values $a = 15.630(2)$ Å, $b = 9.035\ (1)$ Å, $c = 9.154(1)$ Å, $\beta = 124.222(6)°$ in the space group $C2/c$. Presence of some glassy components on top of the pellet is supposed due to a higher background until 0.2 $Å^{-1}$, typical for amorphous admixtures. This monoclinic phase exists approximately until the 2° incidence angle (500 nm thickness of the subsurface layer). Between 0.1° and 0.5°, a smoothing of the background and appearance of another crystalline NaSICON phase with larger lattice parameters is observed, which composition varies with the pellet's depth. Estimation of its lattice parameters at the 1° incidence angle in the same monoclinic $C2/c$ space group gave the values $a = 15.873(3)$ Å, $b = 9.197(2)$ Å, $c = 9.308(2)$ Å, $\beta = 124.207(10)°$. At the pellet depth of about 1 μm (incident angle of 4°), only one NaSICON phase is visible with lattice parameters ($C2/c$ space group) slightly different from the θ-2θ measurement: $a = 15.749(3)$ Å, $b = 9.127(1)$ Å, $c = 9.233(1)$ Å, $\beta = 124.172(10)°$ vs. $a = 15.721(1)$ Å, $b = 9.0938(5)$ Å, $c = 9.2195(5)$ Å, $\beta = 124.184(3)°$.

Apparently, some separation of phases with different compositions occurs in the subsurface region of the pellet during heat treatments at high temperatures and cooling to room temperature. In the near-surface region, a crystalline phase with the highest P- and lowest Si-content exists (assumed as "$Na_2Zr_2SiP_2O_{12}$"), probably together with some amorphous mixed Na-Si-oxides. The subsurface region is characterized by coexistence of "$Na_2Zr_2SiP_2O_{12}$" and a phase with the highest Si- and the lowest P-concentration (assuming the "$Na_{3.9}Zr_2Si_{2.9}P_{0.1}O_{12}$" composition). Interestingly, the composition of "$Na_2Zr_2SiP_2O_{12}$" remains constant, while its amount decreases with pellet depth. In contrast, the composition of the "$Na_{3.9}Zr_2Si_{2.9}P_{0.1}O_{12}$" phase changes with depth, resulting finally in the desired $Na_{3.6}Zr_2Si_{2.6}P_{0.4}O_{12}$ composition.

The XRD pattern of a ground pellet, as shown in Fig. S3, is very close to the grazing incidence diffraction pattern at the incidence angle of 4°. The absence of crystalline Zr-free phases in the XRD patterns suggests that additional phases with almost no Zr, detected by STEM-EELS, are indeed glassy phases. It is evident from these findings that all three NaSICON phases are formed during synthesis and the respective cooling procedure. A detailed analysis of a chemical composition in the surface and subsurface regions of the pellet can be performed using spectroscopy methods, for example, with AES being a suitable technique for depth analysis of the first few nanometers of the pellet.

3.2. Electron beam sensitivity of the NaSICON pellet

Analysis of the NaSICON pellet using AES revealed noticeable changes to the NaSICON surface during the application of the electron beam, as shown in Fig. 2 a-c. Repetitive measurements with the electron beam of 10 μm spot size over a period of 15 min (3 min per measurement) resulted in the formation of a new morphology on top of the NaSICON pellet (Fig. 2d). This new structure grows in blot-like layers and is non-sensitive to the electron beam. Therefore, the elemental composition of this new phase could be determined using EDX as shown in Fig. 2e: it contains only sodium with a most likely adsorbed carbon

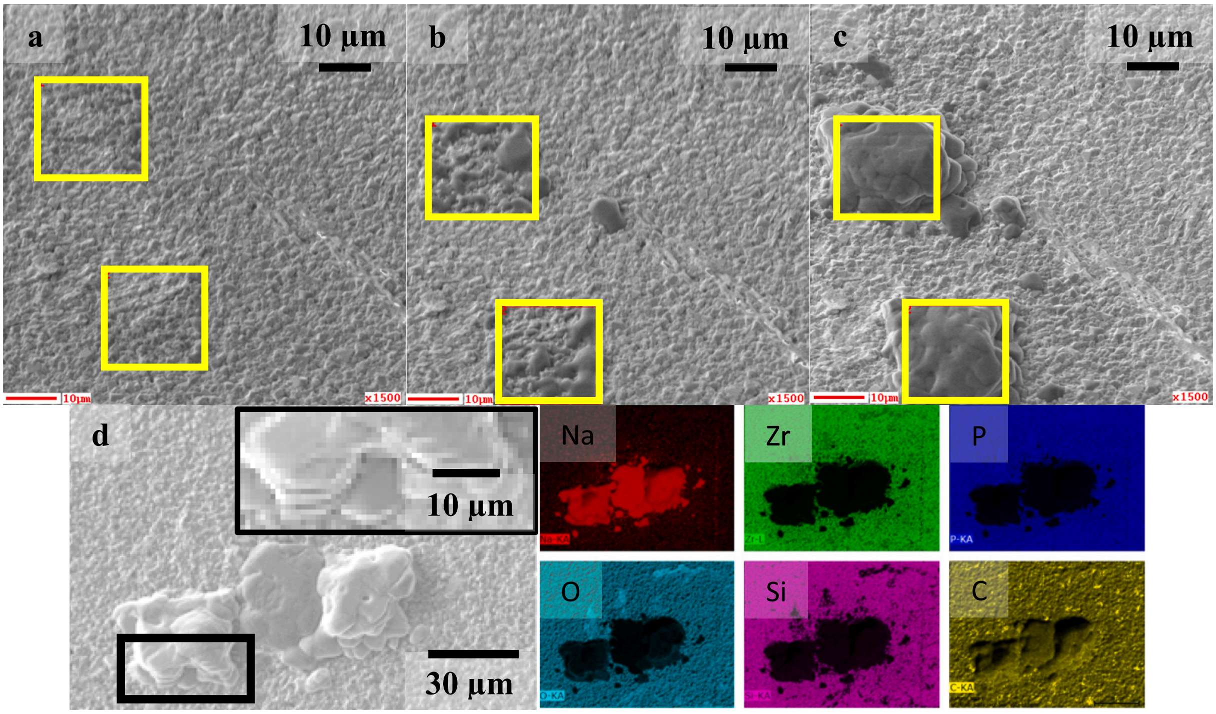

Fig. 2. Series of AES measurements at 5 keV with focus on two rectangular spots. (a) Typical surface morphology of the NaSICON pellet before beam irradiation. (b) First irradiation with a duration of 3 min: formation of a new dark grey structure on the surface, where a direct contact of the electron beam occurred. (c) Growth of the new structure with repetitive measurements. (d) According to EDX analysis, the new structure contains mostly sodium and traces of carbon.

layer. The residual structure, without direct contact to the electron beam, seems to remain intact after beam exposure and growth of the Na-containing new species.

Therefore, the formation of a new sodium-containing phase at the NaSICON surface can be attributed to electron beam irradiation. The beam induces transport of sodium ions due to the formation of a negative center of charge near the surface. As a result, formation of a new sodium-containing phase or even reduction of sodium ions to the metallic state occurs.

This process may also occur when EDX is applied to the surface, resulting in sodium reduction and damage of NaSICON surfaces, as previously described in [22], [31], [48]. Therefore, our further focus was on the impact of EDX measurements on the surface.

Repetitive EDX measurements with 5 kV and 10 nA over a period of 7 h (one hour per measurement) lead to sodium transport to the surface and formation of agglomerates, like in case of AES measurements. The changes on the surface and growing of sodium during recording SEM and EDX are shown in Fig. 3a-c. For other elements see section 5 in the Supporting Information.

Like the behavior during AES measurements, sodium tends to diffuse to the surface and form a new layer on top of the original surface. Due to the larger area during EDX and lower excitation energy, this process is slower in comparison to the growth of metallic sodium during AES measurement. The inhomogeneous growth of sodium indicates that only some areas at the surface were able to collect electrons and establish a center of negative charge.

Subsequent growth of sodium preferentially occurs on already formed structures. Since the growth of the new sodium phase does not cease over time, we assume that the sodium diffuses not only from the areas without beam exposure, but also from the depth of the pellet. Subsequently, stability of the material against the X-ray beam was also verified.

3.3. X-ray beam sensitivity of the NaSICON pellet

To investigate the X-ray stability, a NaSICON pellet was subjected to XPS analysis (at Zr3d, Si2p, O1s, Na1s, P2p and C1s binding energies), which was performed immediately before and after exposure to X-ray radiation for 48 h (Fig. 4). The results showed significant broadening for all measured peaks.

In contrast to AES and EDX, X-ray radiation charges the sample surface positively, causing sodium transport into the depth of the pellet. This behavior is reflected in a partial disappearance of the Na_{KLL} peak at 536 eV, indicating surface Na-depletion. Additionally, the chemical state of other elements on the surface appears to change significantly under X-ray radiation. A possible explanation is the irreversible change of the surface upon the XPS beam.

This assumption is evident in Fig. 4, where broadening of Si2p, O1s, C1s peaks takes place, and peak shifting for P2p, Zr3d, and Na1s occurs. The shift of Zr3d peaks to lower energies and P2p peak to higher energies comes along with the increase in the O1s peak shoulder at 533.2 eV. These changes could be caused by a removal of some oxygen atoms from the crystal structure in the subsurface region. While the shift of Zr3d peaks to lower energies may indicate a partial reduction of Zr^{4+} to form a new Zr^{3+} species, the shift of the P2p peak to higher energies can be explained by shortening the P—O bond length of some P-species due to the moving of the residual oxygen atoms towards positively charged P-centers to compensate the charge. This eventually leads to an increase of the Zr—O bonds as the next neighbor. As a result, a new P2p signal emerges, contributing to the increase in peak width observed in the XPS spectra.

The elongation of the Zr—O bonds supports formation of new Zr^{3+} species together with the original Zr^{4+} state in the spectrum, causing peak broadening towards lower energy. Based on the decreasing Na_{KLL}-Peak in the O1s spectra, it is evident that the sodium content decreases in favor of increasing zirconium and silicon at the surface. The Na1s peak is shifted to lower energy as well, pointing to formation of reduced Na-species (metallization) around the irradiated spot.

Both methods AES/EDX and XPS, employed so far, have irreversibly influenced the surface of NaSICON by inducing local changes in charge centers, accompanied by subsequent sodium ion diffusion. To further investigate this phenomenon, C-AFM was used to examine the NaSICON surface, addressing the question whether it is possible that the electron accumulation takes place at the grain boundaries.

3.4. C-AFM

The C-AFM experiment was performed at ambient conditions. A gold-sputtered backside of the pellet ensured reliable electrical contact with the sample. To measure conductivity, a voltage of 0.2 V was applied to the cantilever. The sample was scanned with the cantilever, and the resulting induced current was measured as a consequence of the potential difference (Fig. 5a). Concurrently, the topography of the sample was also investigated (Fig. 5b).

Notably, significant current flow was observed at grain boundaries in response to the applied voltage. This phenomenon suggests charge

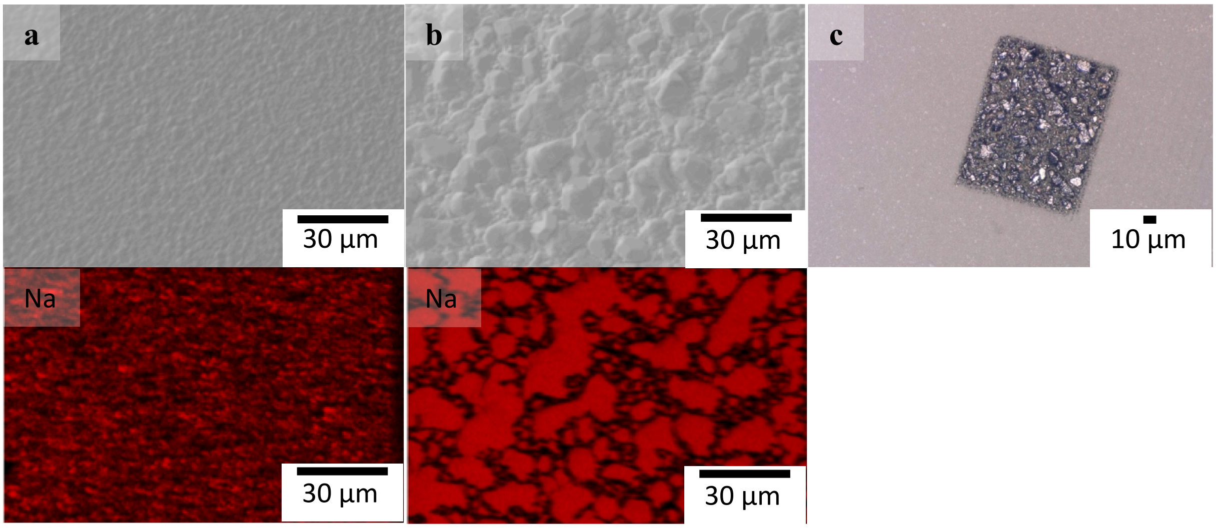

Fig. 3. Results of SEM and EDX measurements of the NaSICON surface after (a) one- and (b) seven-hours measurements. The agglomeration of Na at the surface is clearly visible. (c) The same surface in VHX-6000 microscope clearly shows the metallic luster of sodium.

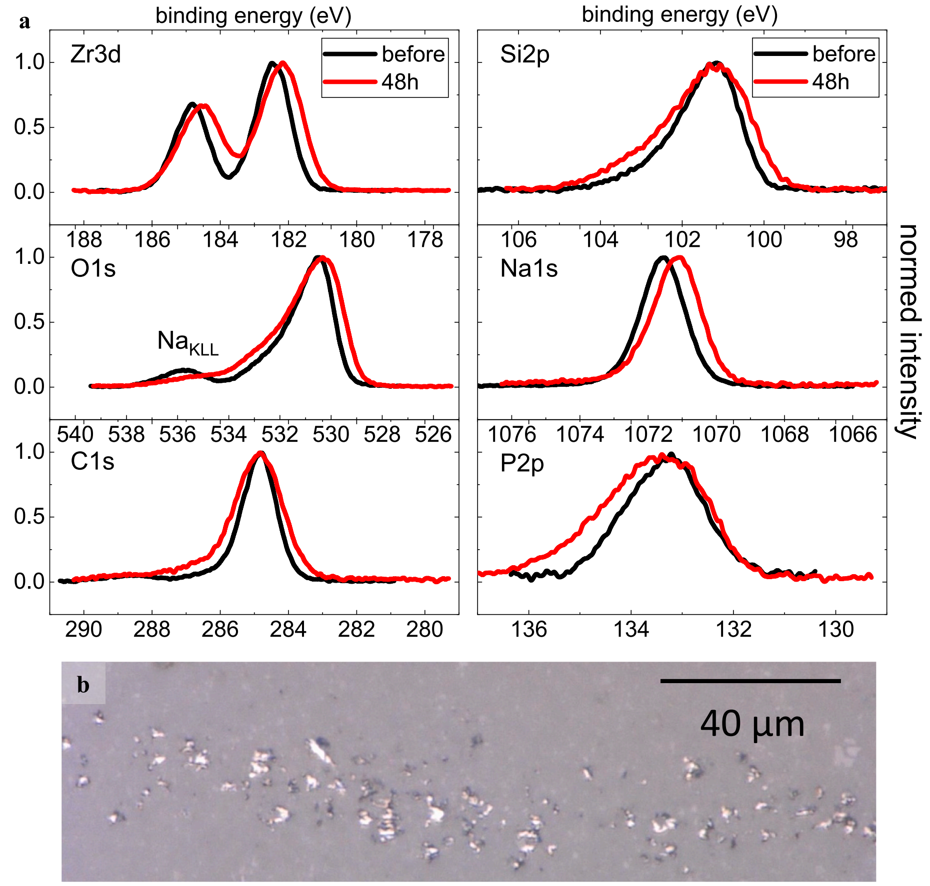

Fig. 4. a) XPS measurements of the NaSICON pellet in the pristine state (black line) and after 48 h exposure to X-ray radiation (red line). A general peak broadening is visible for all detected elements. b) Metallic sodium forms around the irradiated spot size.

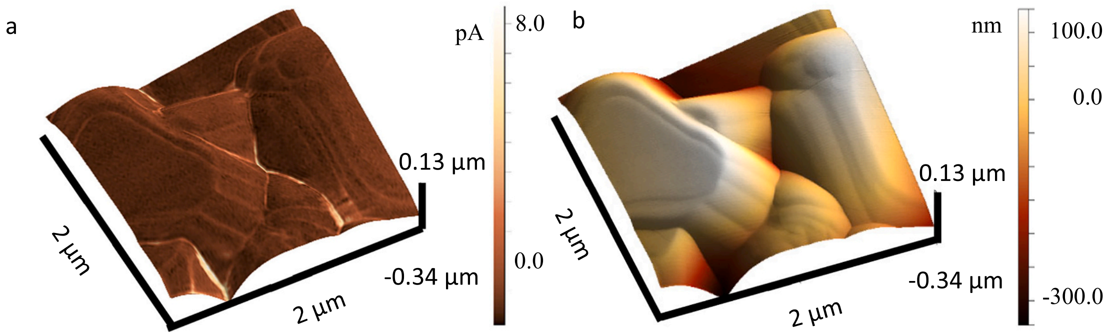

Fig. 5. Combined mapping of the electrical current and topography AFM measurement of a small part of the NaSICON surface. (a) Electrical conductivity is higher at grain boundaries. (b) The topography of the pellet shows a layer-by-layer growth of crystallites at the surface.

movement and, therefore, an electrically conducting phase between the grains. The topography data provided additional insights into crystal growth patterns. Bulk crystals show a layer-by-layer growth, leading to the formation of new grain boundaries along their sides. Interestingly, these grain boundaries accounted for most of the total electrical conductance of the sample. A higher grain than bulk electrical conductivity is typical for insulators [49], a property shared by NaSICON [50]. At this point we want to note that the material investigated in this work shows the typical electrochemical curve in a symmetric Na II Na cell setup (see section 6 in the SI). With this we need to conclude that the formation of metallic sodium at the grain boundaries is an effect not necessarily observable in a electrochemical curve alone.

As it is known, insulators and ceramics accumulate electrons mostly at grain boundaries [51], [52]. Therefore, the observed metallization of sodium in AES, EDX, and XPS measurements should primarily occur at the grain boundaries of the NaSICON material.

3.5. *Stability of NaSICON in contact with sodium*

The stability of NaSICON in contact with metallic sodium is a surface property that warrants more detailed investigations. To this end, we conducted an XPS analysis on a NaSICON surface after one week of intimate contact with metallic sodium. The contact between NaSICON and sodium was achieved by manually pressing NaSICON pieces into sodium metal, without applying additional parameters such as external pressure or temperature. According to theoretical calculations, the formation of reduced P-species like Na_3P should be expected since NaSICON is thermodynamically unstable relative to metallic sodium. [23].

The reduction of phosphorus from +5 to −3 would be experimentally evident through the presence of a new P2p peak at approximately 128 eV in comparison to 133.5 eV for the P^{5+}-species in NaSICON. As shown in Fig. 6a, no peak was observed at this energy, indicating that no reduction of phosphorus took place during simple contact with metallic sodium.

The changes in the XPS spectra are characterized by the disappearance of a shoulder at the O1s and Si2p peak and a slight shift to higher energies in the P2p peak. This phenomenon cannot be attributed to radiation damage, which typically induces substantial peak broadening.

A possible explanation for this observation is the presence of a glassy Si-(P)-O phase at the surface of the NaSICON pellet, seen in STEM-EELS measurements and also mentioned in the literature [53]. The interaction between the metallic sodium and this glassy phase likely leads to the formation of a new Na-Si-(P)-O phase, resulting in disappearance of the shoulder from both Si2p and P2p peaks.

In addition, repeated operando XRD measurements (1 h per range for 68 h) of NaSICON in direct contact with sodium (Fig. 6 b,c) were carried out. No new reflections or shift of existing reflections were observed, pointing to the constant chemical composition of the crystalline phases. However, the reflection intensities of both sodium and NaSICON, increase over time. For sodium, especially the (110) peak grows and becomes a doublet, indicating mass transport and recrystallization of sodium [54].

3.6. Simulation of NaSICON surface properties under beam exposure

Migration of sodium ions towards the surface was observed leading to subsequent sodium metallization when subjected to a high-energy beam exposure, despite any perceived residual charge remaining on the surface. In experimental processes involving electron or high-energy X-ray beams, excess charges can remain close to the upper surface of the material, rendering it positively charged or negatively charged. From a classical perspective, this uncompensated charge forces mobile Na^+ ions from the volume to move towards the negatively charged surface. However, our experiments show that sodium cations appear to move towards the zone of impact regardless of the charge sign on the surface.

Closer examination at the atomic level reveals that the accumulation or depletion of charge density is linked to exact atomic features that accommodate excess charge density. To better understand the influence of terminated atomic groups on charge localization at open surface sites, DFT calculations were conducted using the PBE/PAW level of theory.

The structural features of NaSICON surfaces are currently poorly understood. Two distinct possibilities exist independently of cleavage: unsaturated silicon-oxygen (SiOx)Si- and phosphorus-oxygen (POx)P- bonds in silicon/phosphorus polyhedra, and zirconium-oxygen (ZrOx) Zr- bonds on zirconium sites. Based on a hypothetical model, open bonds to silicon (SiOx)Si- or phosphorus (POx)P- would be less likely formed or persist for long periods of time and participate in quick sodium rearrangement and uptake of oxygen from air. In contrast, oxygen-deficient zirconium polyhedra with unsaturated open bonds and a formal oxidation state of zirconium lower than +4 can exist for a longer period of time. Therefore, in calculations, we considered both scenarios, assuming that environmental oxygen will rapidly refill bonds building fully saturated (SiOx)O- and (POx)O- units. With this in mind, we constructed a NaSICON slab system based on the structure information provided in

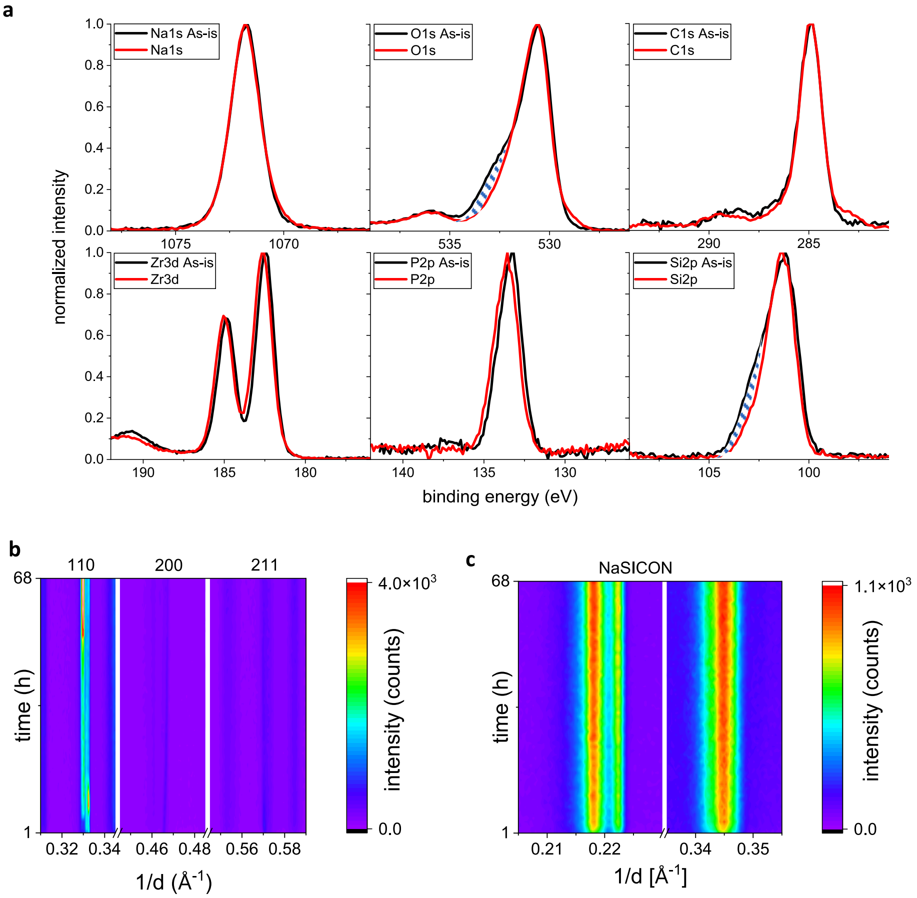

Fig. 6. a) XPS measurements of NaSICON before (black spectra) and after one week in contact with metallic sodium (red spectra). A high-energy shoulder at the Si2p and O1s peaks in the pristine state disappears after one week (shaded area for better clarity). b) Repeated operando XRD measurements of NaSICON in close contact with metallic sodium. Intensity of the (110) Na-peak increases with time, and it becomes a doublet. c) Intensity of NaSICON reflections also increases over time in contact with sodium.

Reference [55]. We built a supercell by repeating the unit cell three times along the c-axis, expanding the natural c-lattice parameter by 10 Å to produce a vacuum of 5 Å on each side.

This arrangement resulted in a thick, symmetric slab exhibiting two distinct types of cleavage on each side: one side features zirconium with untangled bonds, while the other showcases deepened zirconium sites, well-saturated silica, and phosphate polyhedra (Fig. 7). Electronic density was computed without further optimization for the various net charge states. The surface charge states considered were neutral (net charge 0e), two negative (−2e and -4e), and two positive (+2e and + 4e). Bader charges were computed for all systems based on the charge density [56], [57]. This procedure provides a point-charge picture of density accumulation and depletion, tracking the built-in electrostatic potential along the theoretical slab. We also calculated exact differential densities, providing electronic resolution of this property.

Fig. 7 summarizes our results. The molecular orbitals participating in redox processes remain consistent for the selected charge states, and are largely localized around the sides with unsaturated bonds. The point-charge picture aligns with mechanistic expectations for the system. An integral charge would generate either a positive or negative potential around the surface, attracting mobile sodium cations towards the uncompensated charge. When a negative charge is present, significant negative charge accumulates on both surfaces, resulting in a rather symmetric electrostatic potential.

With a net positive charge, the system becomes asymmetric, with one surface maintaining slightly positive charge while the surface featuring (ZrOx)Zr- has nearly neutral charge. Density analysis has shown that the main orbitals, which play a crucial role in charging the surface, have the same topology regardless of the overall net charge. The distribution of charge in a localization scheme is more accurately reflected by local depletion and accumulation of charges than by simply considering integral charges within that scheme. This behavior can be observed through examination of the differential density at the top layer, where primary charge density changes occur near (ZrOx)Zr- bonds.

In these regions, both positive and negative charge bundles are present in the vicinity of untangled bonds. As a result, uncompensated surfaces with (ZrOx)Zr- sites will always exhibit pockets of positive and negative charge densities that cannot be captured by point charge models. Consequently, even when the surface has a net positive or zero charge, patches of negative charge density provide the driving force for mobile sodium cations to move towards the surface.

Experimental conditions like hard X-ray and electron beams allow for building a potential on the surface with a net positive or negative charge. Our simple computational model shows that in both cases; it has the potential to create local charge density pockets promoting Na^+ ion motion towards the surface.

4. Discussion

Upon electron beam and radiation treatment of materials, valence and core electron excitations occur at the surface and subsurface regions, possibly leading to bond breaking, defects formation, ion diffusion, and even to removal of some volatile species. For many non-metallic materials, there are more potentially damaging events as usually supposed. Beam-induced diffusion of mobile ions is a crucial problem in the surface analysis of glasses while beam-induced heating during electron bombardment is very critical for crystalline insulators as well as thin films. A low stability under electron bombardment in AES of ionically bonded solids with the highest valence, in which cations and anions have a difference in Pauling electronegativity higher than 1.7 (for instance, in binary and ternary oxides with Si^{4+}, Ti^{4+}, Nb^{5+} etc.), is demonstrated for some examples in the literature [58].

In the current work, we elucidated the phase composition of the NaSICON surface directly after synthesis, and its interaction with electron beam, X-ray radiation, and metallic sodium. The surface of NaSICON does not represent a single composition and rather consists of multiple stoichiometries, which roughly correspond to temperature-dependent compositions in the calculated phase diagram [26], and some glassy phases. We attribute this phenomenon to different cooling conditions at the surface and in the bulk of the pellet. Faster cooling of the surface compared to the bulk leads to a phase segregation within a depth of at least 1 μm.

In addition, sintering above 1200 °C can lead to depletion of sodium due to evaporation of Na_2O. This process is significantly reduced, but not fully suppressed when the samples are sandwiched between two NaSICON pellets.

Consequently, the surface contains different crystalline NaSICON and glassy phases, primarily responsible for its behavior under beam radiation.

Investigations of the NaSICON surface with SEM, EDX, AES, and XPS result in significant changes in morphology, chemical composition and valence states. Irradiating the surface with the electron beam in routine SEM, EDX, and AES techniques leads to Na^+ diffusion to the surface and sodium metallization. Very likely, the diffusion and metallization start at grain boundaries, where electrons conventionally accumulate in insulators. This grain boundary charge trapping can also explain the

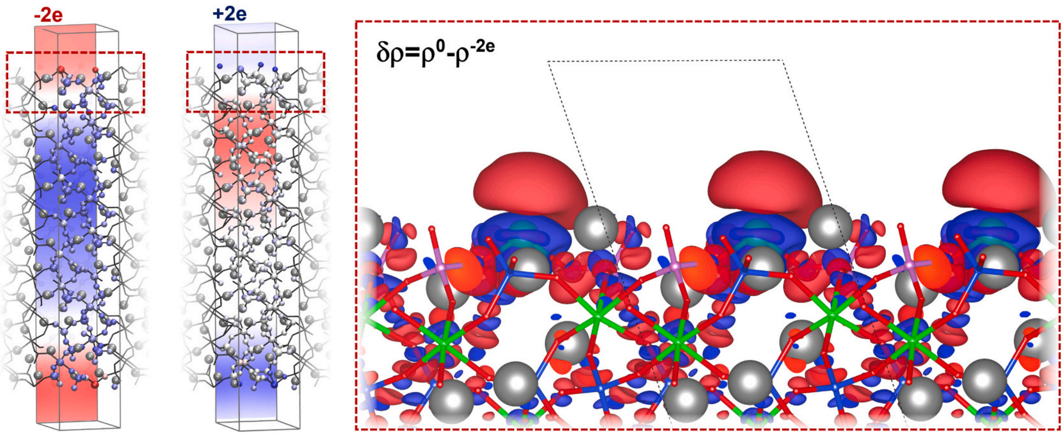

Fig. 7. Column electrostatic potentials (ranging from −50.0 kT/e (red) to +50.0 kT/e (blue), which equals −1.25 V to +1.25 V at $T = 300$ K) calculated using Bader charges for an artificial NASICON slab with net positive (+2e) and net negative (−2e) charges, estimated at the DFT/PAW/PBE level theory. A zoomed region of the top layer of the NASICON slab, highlighted by a red dashed box, illustrates electronic density differences between neutral and net negative (−2e) NASICON systems, showing charge density depletion in blue and accumulation in red. Similarly, charge differences between neutral and the net positive (+2e) system display the same spatial topology, but with reversed signs of depletion and accumulation regions.

observed SEM instability, also known from the literature. [22], [31], [48].

Exposure of NaSICON to X-ray radiation in the XPS technique, which charges the surface positively, leads to Na-depletion on the surface, pointing to Na^+ diffusion into the bulk. However, the remaining Na species are partially reduced as well, as confirmed by the shift of the Na1s peak to lower binding energies.

Our theoretical calculations generally confirm the observed surface degradation of $Na_{3.4}Zr_2Si_{2.4}P_{0.6}O_{12}$. Supposing that the materials surface contains mostly unsaturated $(ZrO_x)Zr$ bonds, a negative charge on the surface during electron irradiation can easily be stabilized through further reduction of Zr, representing a trap for Na^+ cations, accumulated in a subsurface region and even in the bulk. Therefore, a fast Na-diffusion to the surface with the subsequent metallization occurs. A positive charge on the surface from X-ray treatment is partially compensated by unsaturated $(ZrO_x)Zr$ bonds as well, thus mitigating the charge. Simultaneously, a significant negative charge is accumulated in the subsurface region, thus facilitating Na-ion diffusion from the surface into the bulk.

A close contact of metallic sodium to the surface of NaSICON does not reduce phosphorus to valence states below +5. However, some alterations in the chemical surrounding of Si and P were observed, which could be attributed to changes in the composition of glasses on the surface. Additionally, high mobility of metallic sodium at room temperature results in time-dependent material re-distribution in the electrochemical cell with a sandwich-like NaSICON/Na-foil composite. No additional crystalline phases were detected with permanent XRD monitoring during almost 3 days.

In summary, surface investigations using EDX, AES, or XPS analysis may lead to false interpretations of the resulting spectra, if NaSICON is considered as a throughout stable material. It is hardly possible to determine the exact surface composition with these methods. In our experiments on a NaSICON pellet of 1 cm in diameter, we observed damage effects in EDS clearly after 1 h with 5 keV and 10 nA. For AES, the effect was visible already after 3 min measurements with 5 keV and 10 nA. For damage-free results, the applied energy and total measurement time should not exceed these parameters. During XPS measurements, the peak shift of Na and P signals was visible after 45 min of surface radiation.

The recent reports of peak broadening of NaSICON phases need to be re-evaluated in light of these results for prevention of misinterpretations [59], [60], [61].

5. Conclusion

In this work, we investigated surface properties of NaSICON-type pelletized materials with the nominal composition $Na_{3.4}Zr_2Si_{2.4}P_{0.6}O_{12}$ before and after contact with X-rays and electron beam. By combination of STEM-EELS and grazing incidence diffraction, which could clearly show that the pellets represent a single-phase material deeper than approximately 1 μm, while multiple crystalline and amorphous phases coexist at the surface and in the subsurface region, probably because of the heat treatment and cooling processes during the preparation procedure. The interaction of the electron beam with the surface of the material during a conventional measuring procedure result in deposition of metallic sodium onto the surface. The presence of glassy phases facilitates sodium metallization, although destroying the NaSICON crystal structure upon negative charging the surface should occur as well, as shown by theoretical calculations. Interaction of the surface with X-ray beam during XPS measurements (binding energy interval between 95 and 1080 eV) results in sodium depletion in the area under direct contact with the beam, but sodium metallization around, again in accordance with theoretical considerations. The close contact of metallic sodium to the NaSICON surface has an impact on the chemical state of Si-, O- and Na-species, which are probably components of amorphous phases. As a next step, surface changes of NaSICON pellets should be evaluated after applying current/voltage in symmetric Na || NaSICON || Na cells.

CRediT authorship contribution statement

Alexander Thomas: Writing – original draft, Visualization, Investigation, Conceptualization. **Björn Pohle:** Validation, Investigation. **Martin Hantusch:** Resources, Methodology, Investigation. **Johannes Schultz:** Visualization, Methodology, Investigation. **Stas Avdoshenko:** Visualization, Software, Investigation. **Ronny Buckan:** Investigation. **Lars Giebeler:** Investigation. **Thomas Mühl:** Investigation. **Monika Bhardwaj:** Resources. **Frank Tietz:** Resources. **Jörg Feller:** Writing – review & editing, Validation, Supervision, Methodology. **Stefan Kaskel:** Writing – review & editing, Supervision, Methodology. **Daria Mikhailova:** Writing – review & editing, Validation, Supervision, Methodology, Funding acquisition.

Declaration of competing interest

The authors declare that they have no known competing financial interests or personal relationships that could have appeared to influence the work reported in this paper.

Acknowledgements

This work was supported by the *Bundesministerium für Forschung, Technologie und Raumfahrt* and was carried out as part of the HeNa project (support codes: 03XP0390B and 03XP0390C). The authors take responsibility for the content of this publication.

Johannes Schultz thanks the HORIZON EUROPE framework program, grant number 101094299, for financial support. The authors thank Thomas Wiek for the FIB section of the NaSICON material, Andrea Voß and Anne Voidel (all IFW Dresden) for support and discussion of results of various measurements.

Appendix A. Supplementary data

Supplementary data to this article can be found online at https://doi.org/10.1016/j.cej.2026.175127.

Data availability

Data will be made available on request.

References

[1] T. Kim, W. Song, D.-Y. Son, L.K. Ono, Y. Qi, Lithium-ion batteries: outlook on present, future, and hybridized technologies, J. Mater. Chem. A 7 (7) (2019) 2942–2964, https://doi.org/10.1039/C8TA10513H.

[2] E.A. Olivetti, G. Ceder, G.G. Gaustad, X. Fu, Lithium-Ion Battery Supply Chain Considerations: Analysis of Potential Bottlenecks in Critical Metals, Joule 1 (2) (2017) 229–243, https://doi.org/10.1016/j.joule.2017.08.019.

[3] H. Vikström, S. Davidsson, M. Höök, Lithium availability and future production outlooks, Appl. Energy 110 (2013) 252–266, https://doi.org/10.1016/j.apenergy.2013.04.005.

[4] C. Delmas, Sodium and Sodium-Ion Batteries: 50 Years of Research, Adv. Energy Mater. 8 (17) (2018) 1703137, https://doi.org/10.1002/aenm.201703137.

[5] L. Zhao, et al., Engineering of Sodium-Ion Batteries: Opportunities and Challenges, Engineering 24 (2023) 172–183, https://doi.org/10.1016/j.eng.2021.08.032.

[6] N. Tapia-Ruiz, et al., 2021 roadmap for sodium-ion batteries, J. Phys. Energy 3 (3) (2021) 031503, https://doi.org/10.1088/2515-7655/ac01ef.

[7] J. Janek, W.G. Zeier, A solid future for battery development, Nat. Energy 1, no. 9, Art. no. 9 (2016), https://doi.org/10.1038/nenergy.2016.141.

[8] E. Kartini, C.T. Genardy, The Future of All Solid State Battery, IOP Conf. Ser.: Mater. Sci. Eng. 924 (1) (2020) 012038, https://doi.org/10.1088/1757-899X/924/1/012038.

[9] C. Wang, X. Sun, The Promise of Solid-State Batteries for Safe and Reliable Energy Storage, Engineering 21 (2023) 32–35, https://doi.org/10.1016/j.eng.2022.10.008.

[10] D. Wu, F. Wu, Toward better batteries: Solid-state battery roadmap 2035+, eTransportation 16 (2023) 100224 https://doi.org/10.1016/j.etran.2022.100224.

[11] C.L. Dirksen, K. Skadell, M. Schulz, M. Stelter, Effects of TiO_2 doping on Li^+-stabilized Na-β″-alumina for energy storage applications, Sep. Purif. Technol. 213 (2019) 88–92, https://doi.org/10.1016/j.seppur.2018.12.028.

[12] M.P. Fertig, C. Dirksen, K. Skadell, M. Schulz, M. Stelter, Sodium-Beta Alumina and Its Application in a Novel Sodium-Based Solid-State Cell Concept, ECS Meet. Abstr. MA2023–01, no. 6 (2023) 1000, https://doi.org/10.1149/MA2023-0161000mtgabs.

[13] H.U. Beyeler, R.D. Shannon, H.Y. Chen, Ionic conductivity of single-crystal $Na_5YSi_4O_{12}$, Appl. Phys. Lett. 37 (10) (1980) 934–935, https://doi.org/10.1063/1.91765.

[14] A. Hayashi, K. Noi, N. Tanibata, M. Nagao, M. Tatsumisago, High sodium ion conductivity of glass–ceramic electrolytes with cubic Na_3PS_4, J. Power Sources 258 (2014) 420–423, https://doi.org/10.1016/j.jpowsour.2014.02.054.

[15] R. Černý, F. Murgia, M. Brighi, Metal hydroborates: From hydrogen stores to solid electrolytes, J. Alloys Compd. 895 (2022) 162659, https://doi.org/10.1016/j.jallcom.2021.162659.

[16] R.P. S, V. Prasannavenkadesan, V. Katiyar, A.S. Achalkumar, Polymer electrolytes: evolution, challenges, and future directions for lithium-ion batteries, RSC Appl. Polym. 3 (3) (2025) 499–531, https://doi.org/10.1039/D4LP00325J.

[17] F. Tietz, Phase relations of NASICON materials and compilation of the quaternary phase diagram Na_2O-P_2O_5-SiO_2-ZrO_2, AIMS Mater. Sci. 4 (6) (2017) 1305–1318, https://doi.org/10.3934/matersci.2017.6.1305.

[18] Q. Ma, et al., Enhancing the Dendrite Tolerance of NaSICON Electrolytes by Suppressing Edge Growth of Na Electrode along Ceramic Surface, Adv. Energy Mater. 12 (40) (2022) 2201680, https://doi.org/10.1002/aenm.202201680.

[19] T. Lan, et al., Room-temperature all-solid-state sodium batteries with robust ceramic interface between rigid electrolyte and electrode materials, Nano Energy 65 (2019) 104040, https://doi.org/10.1016/j.nanoen.2019.104040.

[20] Q. Ma, C.-L. Tsai, X.-K. Wei, M. Heggen, F. Tietz, J.T.S. Irvine, Room temperature demonstration of a sodium superionic conductor with grain conductivity in excess of 0.01 S cm^{-1} and its primary applications in symmetric battery cells, J. Mater. Chem. A 7 (13) (2019) 7766–7776, https://doi.org/10.1039/C9TA00048H.

[21] Udo Warhus, Synthese und Stabilität des NaSICON Mischkristallsystems ($Na_{1+x}Zr_2Si_xP_{3-x}O_{12}$, $0 \le x \le 3$), Universität Stuttgart, Suttgart, 1986.

[22] H. Schmid, L.C. De Jonghe, C. Cameron, Chemical stability of Nasicon, Solid State Ionics 6 (1) (1982) 57–63, https://doi.org/10.1016/0167-2738(82)90096-0.

[23] J. Maier, U. Warhus, E. Gmelin, Thermodynamic and electrochemical investigations of the Nasicon solid solution system, Solid State Ionics 18–19 (1986) 969–973, https://doi.org/10.1016/0167-2738(86)90294-8.

[24] F. Tietz, et al., Impact of Microstructural Properties on Ionic and Heat Transport in NaSICON Glass Ceramics, Batteries Supercaps 8 (6) (2025) e202500093, https://doi.org/10.1002/batt.202500093.

[25] U. Warhus, J. Maier, A. Rabenau, Thermodynamics of NASICON ($Na_{1+x}Zr_2Si_xP_{3-x}O_{12}$), J. Solid State Chem. 72 (1) (1988) 113–125, https://doi.org/10.1016/0022-4596(88)90014-X.

[26] Z. Deng, et al., Phase Behavior in Rhombohedral NaSiCON Electrolytes and Electrodes, Chem. Mater. 32 (18) (2020) 7908–7920, https://doi.org/10.1021/acs.chemmater.0c02695.

[27] A.G. Jolley, D.D. Taylor, N.J. Schreiber, E.D. Wachsman, Structural Investigation of Monoclinic-Rhombohedral Phase Transition in $Na_3Zr_2Si_2PO_{12}$ and Doped NASICON, J. Am. Ceram. Soc. 98 (9) (2015) 2902–2907, https://doi.org/10.1111/jace.13692.

[28] W. Zhou, Y. Li, S. Xin, J.B. Goodenough, Rechargeable Sodium All-Solid-State Battery, ACS Cent. Sci. 3 (1) (2017) 52–57, https://doi.org/10.1021/acscentsci.6b00321.

[29] S. Oswald, Auger- and X-ray Photoelectron Spectroscopy at Metallic Li Material: Chemical Shifts Related to Sample Preparation, Gas Atmosphere, and Ion and Electron Beam Effect, Batteries 8, no. 3, Art. no. 3 (2022), https://doi.org/10.3390/batteries8030024.

[30] S. Oswald, T. Schmeida, D. Mikhailova, Model experiments with Auger electron and X-ray photoelectron spectroscopy at lithiated graphite material: Surface changes related to ion- and electron-beam effects, Appl. Surf. Sci. 619 (2023) 156776, https://doi.org/10.1016/j.apsusc.2023.156776.

[31] F. Tietz, J. Koepke, W. Urland, Analytical investigations of β-Al2O3 and β″-Al2O3 crystals, J. Cryst. Growth 118 (3) (1992) 314–318, https://doi.org/10.1016/0022-0248(92)90078-W.

[32] A. Cros, Charging effects in X-ray photoelectron spectroscopy, J. Electron Spectrosc. Relat. Phenom. 59 (1) (1992) 1–14, https://doi.org/10.1016/0368-2048(92)85008-U.

[33] D.R. Baer, et al., XPS guide: Charge neutralization and binding energy referencing for insulating samples, J. Vac. Sci. Technol. A 38 (3) (2020) 031204, https://doi.org/10.1116/6.0000057.

[34] K. Yasuda, J.-M. Costantini, G. Baldinozzi, 1.06 - Radiation-Induced Effects on Material Properties of Ceramics: Mechanical and Dimensional Properties☆, in: R.J. M. Konings, R.E. Stoller (Eds.), Comprehensive Nuclear Materials, Second edition, Elsevier, Oxford, 2020, pp. 153–185, https://doi.org/10.1016/B978-0-12-803,581-8.12052-1.

[35] Q. Ma, M. Guin, S. Naqash, C.-L. Tsai, F. Tietz, O. Guillon, Scandium-Substituted $Na_3Zr_2(SiO_4)_2(PO_4)$ Prepared by a Solution-Assisted Solid-State Reaction Method as Sodium-Ion Conductors, Chem. Mater. 28 (13) (2016) 4821–4828, https://doi.org/10.1021/acs.chemmater.6b02059.

[36] S. Naqash, Q. Ma, F. Tietz, O. Guillon, $Na_3Zr_2(SiO_4)_2(PO_4)$ prepared by a solution-assisted solid state reaction, Solid State Ionics 302 (2017) 83–91, https://doi.org/10.1016/j.ssi.2016.11.004.

[37] T. Roisnel, J. Rodríquez-Carvajal, WinPLOTR: A Windows Tool for Powder Diffraction Pattern Analysis, Mater. Sci. Forum 378–381 (2001) 118–123, https://doi.org/10.4028/www.scientific.net/MSF.378-381.118.

[38] G. Kresse, J. Hafner, Ab initio molecular dynamics for liquid metals, Phys. Rev. B 47 (1) (1993) 558–561, https://doi.org/10.1103/PhysRevB.47.558.

[39] E. Zirngiebl, et al., Crystal-field excitations in CeB_6 studied by Raman and neutron spectroscopy, Phys. Rev. B 30 (7) (1984) 4052–4054, https://doi.org/10.1103/PhysRevB.30.4052.

[40] E. Zirngiebl, et al., New crystal field level scheme of CeB_6 deduced from Raman and neutron spectroscopy, J. Appl. Phys. 57 (8) (1985) 3769, https://doi.org/10.1063/1.334967.

[41] R.F.W. Bader, P.M. Beddall, P.E. Cade, Partitioning and characterization of molecular charge distributions, J. Am. Chem. Soc. 93 (13) (1971) 3095–3107, https://doi.org/10.1021/ja00742a001.

[42] A. Hjorth Larsen, et al., The atomic simulation environment—a Python library for working with atoms, J. Phys. Condens. Matter 29 (27) (2017) 273002, https://doi.org/10.1088/1361-648X/aa680e.

[43] Z. Deng, et al., Fundamental investigations on the sodium-ion transport properties of mixed polyanion solid-state battery electrolytes, Nat. Commun. 13 (1) (2022) 4470, https://doi.org/10.1038/s41467-022-32,190-7.

[44] A. Krajewski, R. Valmori, A. Fiegna, Some crystallographic trends into the $Na_{1+x}Zr_2Si_xP_{3-x}O_{12}$ System, Cryst. Res. Technol. 19 (7) (1984) 893–903, https://doi.org/10.1002/crat.2170190705.

[45] D. Simeone, G. Baldinozzi, D. Gosset, S. Le Caer, J.-F. Bérar, Grazing incidence X-ray diffraction for the study of polycrystalline layers, Thin Solid Films 530 (2013) 9–13, https://doi.org/10.1016/j.tsf.2012.07.068.

[46] A.L. Bail, Whole powder pattern decomposition methods and applications: A retrospection, Powder Diffract. 20 (4) (2005) 316–326, https://doi.org/10.1154/1.2135315.

[47] H.Y.-P. Hong, Crystal structures and crystal chemistry in the system $Na_{1+x}Zr_2Si_xP_{3-x}O_{12}$, Mater. Res. Bull. (1976), https://doi.org/10.1016/0025-5408(76)90073-8.

[48] Z. Ding, et al., Exploring the influence of focused ion beam processing and scanning electron microscopy imaging on solid-state electrolytes, Microscopy 72 (4) (2023) 326–335, https://doi.org/10.1093/jmicro/dfac064.

[49] G. Lormand, ELECTRICAL PROPERTIES OF GRAIN BOUNDARIES, J. Phys. Colloq. 43 (C6) (1982) C6–292, https://doi.org/10.1051/jphyscol:1982625.

[50] E. Quérel, I.D. Seymour, A. Cavallaro, Q. Ma, F. Tietz, A. Aguadero, The role of NaSICON surface chemistry in stabilizing fast-charging Na metal solid-state batteries, J. Phys. Energy 3 (4) (2021) 044007, https://doi.org/10.1088/2515-7655/ac2fb3.

[51] K.S.N. Vikrant, R.E. García, Charged grain boundary transitions in ionic ceramics for energy applications, npj Comput. Mater. 5, no. 1, Art. no. 1 (2019), https://doi.org/10.1038/s41524-019-0159-2.

[52] S.K. Wallace, K.P. McKenna, Grain Boundary Controlled Electron Mobility in Polycrystalline Titanium Dioxide, Adv. Mater. Interfaces 1 (5) (2014) 1400078, https://doi.org/10.1002/admi.201400078.

[53] H. Liu, Y. Xing, N. Chen, J. Wu, Y. Li, C. Zhang, Engineering the NASICON Electrolyte/Na Anode Interface by Tuning the Phase of Electrolyte for Solid-State Sodium Battery, Chem. Mater. 35 (20) (2023) 8686–8694, https://doi.org/10.1021/acs.chemmater.3c01922.

[54] A. Thomas, B. Pohle, J. Schultz, M. Hantusch, D. Mikhailova, NaOH protective layer for a stable sodium metal anode in liquid electrolytes, J. Energy Storage 77 (2024) 109900, https://doi.org/10.1016/j.est.2023.109900.

[55] N.G. Bukun, I.A. Domashnev, E.I. Moskvina, E.A. Ukshe, Synthesis and electric conductivity of a NASICON-type electrolyte, Inorg. Mater. Engl. Transl. U. S. 24 (3) (1988). Accessed: Jul. 05, 2025. [Online]. Available: https://www.osti.gov/biblio/6293352.

[56] R.F.W. Bader, Atoms in Molecules: A Quantum Theory, Oxford University Press (1990), https://doi.org/10.1093/oso/9780198551683.001.0001.

[57] W. Tang, E. Sanville, G. Henkelman, A grid-based Bader analysis algorithm without lattice bias, J. Phys. Condens. Matter Inst. Phys. J. 21 (8) (2009) 084204, https://doi.org/10.1088/0953-8984/21/8/084204.

[58] C.G. Pantano, T.E. Madey, Electron beam damage in Auger electron spectroscopy, Appl. Surf. Sci. 7, no. 1, Art. no. 1 (1981), https://doi.org/10.1016/0378-5963(81)90065-9.

[59] T. Ortmann, et al., Kinetics and Pore Formation of the Sodium Metal Anode on NASICON-Type $Na_{3.4}Zr_2Si_{2.4}P_{0.6}O_{12}$ for Sodium Solid-State Batteries, Adv. Energy Mater. 13 (5) (2023) 2202712, https://doi.org/10.1002/aenm.202202712.

[60] W. Wang, S. Hu, Z. Jian, W. Chen, Insight into the Evolution of Voids at the NASICON/Na Interface and Suppressing Void Accumulation by a Semiliquid Wetting Strategy, ACS Appl. Energy Mater. 6 (15) (2023) 7837–7846, https://doi.org/10.1021/acsaem.3c00601.

[61] E. Quérel, N.J. Williams, I.D. Seymour, S.J. Skinner, A. Aguadero, Operando Characterization and Theoretical Modeling of Metal|Electrolyte Interphase Growth Kinetics in Solid-State Batteries. Part I: Experiments, Chem. Mater. 35 (3) (2023) 853–862, https://doi.org/10.1021/acs.chemmater.2c03130.